

MIT Open Access Articles

NUMERICAL SIMULATION OF HOT ACCRETION FLOWS. III. REVISITING WIND PROPERTIES USING THE TRAJECTORY APPROACH

The MIT Faculty has made this article openly available. *Please share* how this access benefits you. Your story matters.

Citation: Yuan, Feng, Zhaoming Gan, Ramesh Narayan, Aleksander Sadowski, Defu Bu, and Xue-Ning Bai. "NUMERICAL SIMULATION OF HOT ACCRETION FLOWS. III. REVISITING WIND PROPERTIES USING THE TRAJECTORY APPROACH." *The Astrophysical Journal* 804, no. 2 (May 6, 2015): 101. © 2015 The American Astronomical Society

As Published: <http://dx.doi.org/10.1088/0004-637x/804/2/101>

Publisher: IOP Publishing

Persistent URL: <http://hdl.handle.net/1721.1/98370>

Version: Final published version: final published article, as it appeared in a journal, conference proceedings, or other formally published context

Terms of Use: Article is made available in accordance with the publisher's policy and may be subject to US copyright law. Please refer to the publisher's site for terms of use.



NUMERICAL SIMULATION OF HOT ACCRETION FLOWS. III. REVISITING WIND PROPERTIES USING THE TRAJECTORY APPROACH

FENG YUAN¹, ZHAOMING GAN¹, RAMESH NARAYAN², ALEKSANDER SADOWSKI^{3,4}, DEFU BU¹, AND XUE-NING BAI^{2,5}

¹ Shanghai Astronomical Observatory, Chinese Academy of Sciences, 80 Nandan Road, Shanghai 200030, China;

fyuan@shao.ac.cn (FY), zmgan@shao.ac.cn (ZG), dfbu@shao.ac.cn (DB)

² Harvard-Smithsonian Center for Astrophysics, 60 Garden Street, Cambridge, MA 02138, USA;

narayan@cfa.harvard.edu (RN), xbai@cfa.harvard.edu (XNB)

³ MIT Kavli Institute for Astrophysics and Space Research, USA; asadowsk@mit.edu

Received 2014 December 26; accepted 2015 February 5; published 2015 May 6

ABSTRACT

Previous MHD simulations have shown that wind must exist in black hole hot accretion flows. In this paper, we continue our study by investigating the detailed properties of wind and the mechanism of wind production. For this aim, we make use of a 3D general relativistic MHD simulation of hot accretion flows around a Schwarzschild black hole. To distinguish real wind from turbulent outflows, we track the trajectories of the virtual Lagrangian particles from simulation data. We find two types of real outflows, i.e., a jet and a wind. The mass flux of wind is very significant, and its radial profile can be described by $\dot{M}_{\text{wind}} \approx \dot{M}_{\text{BH}}(r/20 r_s)$, with \dot{M}_{BH} being the mass accretion rate at the black hole horizon and r_s being the Schwarzschild radius. The poloidal wind speed almost remains constant once they are produced, but the flux-weighted wind speed roughly follows $v_{p,\text{wind}}(r) \approx 0.25v_k(r)$, with $v_k(r)$ being the Keplerian speed at radius r . The mass flux of the jet is much lower, but the speed is much higher, $v_{p,\text{jet}} \sim (0.3\text{--}0.4)c$. Consequently, both the energy and momentum fluxes of the wind are much larger than those of the jet. The wind is produced and accelerated primarily by the combination of centrifugal force and magnetic pressure gradient, while the jet is mainly accelerated by the magnetic pressure gradient. Finally, we find that the wind production efficiency $\epsilon_{\text{wind}} \equiv \dot{E}_{\text{wind}}/\dot{M}_{\text{BH}}c^2 \sim 1/1000$ is in good agreement with the value required from large-scale galaxy simulations with active galactic nucleus feedback.

Key words: accretion, accretion disks – black hole physics – galaxies: jets – hydrodynamics

1. INTRODUCTION

Black hole accretion models can be divided into two classes based on the temperature of the accretion flow. One is cold accretion models such as the standard thin disk (Shakura & Sunayev 1973; Pringle 1981); the other is the hot accretion flow such as advection-dominated accretion flow (Narayan & Yi 1994, 1995; see Yuan & Narayan 2014 for the recent review of the theory of hot accretion flow and its applications). Hot accretion flows are believed to exist in low-luminosity active galactic nuclei (AGNs), which likely reside in the majority of galaxies, and hard/quiescent states of black hole X-ray binaries. One important question in the study of hot accretion flows in recent years is related to winds, i.e., uncollimated mass outflow. On the one hand, whether winds are present or not is a fundamental question in the dynamics of accretion, and the presence of wind helps explain many observations, including the spectrum of black hole sources (e.g., Yuan et al. 2003), emission lines from accretion flow (e.g., Wang et al. 2013), the *Fermi* bubbles in the Galactic center (Mou et al. 2014), and perhaps even some direct observations on outflow (e.g., Crenshaw et al. 2003; Tombesi et al. 2010, 2014; Crenshaw & Kraemer 2012; Yuan et al. 2012a). On the other hand, AGN feedback is widely believed to play a crucial role in galaxy formation and evolution (Fabian 2012; Kormendy & Ho 2013), while winds produced by the AGN accretion flow are one of the most important ingredients for such feedback because they could interact with the interstellar medium (ISM)

in the host galaxy by exchanging momentum and depositing energy (King 2003; Ciotti et al. 2010; Debuhr et al. 2010; Ostriker et al. 2010; Novak et al. 2011; Gan et al. 2014). The aim of the present work is to understand the detailed wind properties from accretion flow, which will provide important input for studies of AGN feedback.

The study of winds from hot accretion flows can be traced back to Stone et al. (1999; see also Igumenshchev & Abramowicz 1999, 2000). They performed the first global hydrodynamical numerical simulation of hot accretion flow and calculated the following time-averaged radial profiles of inflow and outflow rates:

$$\dot{M}_{\text{in}}(r) = 2\pi r^2 \left\langle \int_0^\pi \rho \min(v_r, 0) \sin \theta d\theta \right\rangle_{t\phi}, \quad (1)$$

$$\dot{M}_{\text{out}}(r) = 2\pi r^2 \left\langle \int_0^\pi \rho \max(v_r, 0) \sin \theta d\theta \right\rangle_{t\phi}, \quad (2)$$

where the angle brackets represent time averages (and also average over the azimuthal angle ϕ in the case of 3D simulations). We emphasize this point because the order of doing the time average and the integral will make significant differences, as we will show later in this paper. Note also that the outflow rate calculated by Equation (2) does not necessarily represent the mass flux of “real outflow,” because the positive radial velocity may just come from the turbulent motion of the accretion flow. The most important result they obtained is that the inflow rate based on Equation (1) follows a power-law

⁴ NASA Einstein Fellow.

⁵ NASA Hubble Fellow.

function of radius,

$$\dot{M}_{\text{in}}(r) = \dot{M}_{\text{in}}(r_{\text{out}}) \left(\frac{r}{r_{\text{out}}} \right)^s. \quad (3)$$

Here $\dot{M}_{\text{in}}(r_{\text{out}})$ is the mass inflow rate at the outer boundary r_{out} . The radial dynamical range of this simulation is rather small, spanning about two orders of magnitude in radius. But the results were later confirmed by simulations with a much larger radial dynamical range of four orders of magnitude (Yuan et al. 2012b). Moreover, MHD simulations yield very similar results that typically $s \sim 0.5-1$ (e.g., Stone & Pringle 2001; Hawley & Balbus 2002; Igumenshchev et al. 2003; Pen et al. 2003; see review in Yuan et al. 2012b).

It is exciting to note that the predicted inward decrease of accretion rate has recently been confirmed by two observations; both are on Sgr A*. One is the detection of radio polarization at a level of 2%–9% (e.g., Aitken et al. 2000; Bower et al. 2003; Marrone et al. 2007). Such high polarization requires that the mass accretion rate close to the black hole horizon must be within a certain range, which is two orders of magnitude lower than the Bondi rate obtained from *Chandra* observations. The other evidence is from the *Chandra* observation of the iron emission lines that originated from the hot accretion flow (Wang et al. 2013). The modeling to the $K\alpha$ lines indicates a flat radial density profile near the Bondi radius, which confirms that the mass accretion rate decreases with decreasing radius. This is because if the mass accretion rate were a constant of radius, the density profile would be much steeper.

Two competing models have been proposed to explain the above numerical simulation result. In the adiabatic inflow-outflow solution, the inward decrease of mass accretion rate is due to the mass lost in the wind (Blandford & Begelman 1999, 2004; Begelman 2012). In the early works of Blandford & Begelman (1999, 2004), the value of parameter s in Equation (3) is a free parameter. But in the more recent work of Begelman (2012), the value of s is argued to be close to unity. The other model is the convection-dominated accretion flow (CDAF) model. In this model, the accretion flow is assumed to be convectively unstable. The inward decrease of accretion rate is explained as more and more gas is locked in convective eddies (Narayan et al. 2000; Quataert & Gruzinov 2000; Abramowicz et al. 2002; Igumenshchev 2002). For a long time, it is unclear which scenario is physical.

Three numerical simulation works have been conducted to investigate this problem (Narayan et al. 2012; Yuan et al. 2012a; Li et al. 2013). Both Narayan et al. (2012) and Yuan et al. (2012a) found that the hot accretion flow is convectively stable. This indicates that the CDAF model may not apply, leaving outflow/wind as the only possible solution. The fundamental question is how strong the wind is. Narayan et al. (2012) calculated the outflow rate based on Equation (2), except that they move the $t\phi$ average inside the integral. Although this calculation underestimates the mass flux of real outflow, as we will show later in this paper, it eliminates contributions from turbulent motion and produces substantially lower outflow rate than Equation (2). In fact, only an upper limit was reported since the outflow rate was found to not converge with time. On the other hand, Yuan et al. (2012a) systematically compared the properties of inflow and outflow, such as angular momentum and temperature, and found that

they are quite different. They therefore concluded that systematic outflow must exist and the outflow rate must be a significant fraction of that indicated by Equation (2). They argued that the rather weak outflow rate obtained in Narayan et al. (2012) is because outflow is intrinsically instantaneous. The outflow stream can wander around in 3D space and thus will be canceled if the time average is performed first. Their work indicates that the mass lost via the wind is the reason for the inward decrease of the accretion rate (Equation (3)). The hydrodynamical simulations by Li et al. (2013) obtained a similar conclusion to Yuan et al. (2012a). Begelman (2012) and Gu (2014) studied why winds should exist in hot accretion flows.

The aim of the present work is twofold. First, Yuan et al. (2012a) showed the existence of outflow only based on some indirect arguments, so it is necessary to show the existence of wind in a more direct way. Second, we want to quantitatively calculate the properties of wind, including the mass flux, angular distribution, and velocity. These properties are especially important to determining how effective the interaction between wind and ISM is. The amount of mass flux of wind is also useful to resolve the discrepancy on the mass flux of wind between Narayan et al. (2012) and Yuan et al. (2012a). Sadowski et al. (2013) have also studied the properties of wind and jets under various parameters such as black hole spin. As with Narayan et al. (2012), their calculations are based on the time-averaged quantities and thus may only give a lower limit.

We use a “trajectory” approach in this work for our above-mentioned aims. That is, we use the numerical simulation data of hot accretion flow to follow the trajectories of some “test particles” so as to see whether the particles can really escape or simply have turbulent motions, and we further calculate the properties of the wind. The paper is organized as follows. In Section 2, we will describe the simulation data based on which we perform the analysis, and the “trajectory” method we use. The results are presented in Section 3. Section 4 is devoted to the analysis of the acceleration mechanism of wind. We then summarize and conclude in Section 5.

2. SIMULATION DATA AND THE TRAJECTORY METHOD

2.1. Simulation Data of Hot Accretion Flow Models

We have considered two different simulations to perform the “trajectory” analysis. One is the 2D MHD simulation described in Yuan et al. (2012a), and the other is the 3D GRMHD simulation described in Narayan et al. (2012). In the former, the initial condition is a rotating torus with constant specific angular momentum. The density maximum is located at $r = 100 r_s$, where $r_s \equiv 2 r_g \equiv 2 GM/c^2$. The initial magnetic field is poloidal, a single set of loops confined to the interior of the torus, and the loops are parallel to the density loops. The simulation is performed using the ZEUS code. The readers are referred to Yuan et al. (2012a) for details. In the second simulation, the initial condition is again a rotating torus, but the details of the torus are different. It has inner and outer edges at $r_{\text{in}} = 10 r_g$ and $r_{\text{out}} = 1000 r_g$, respectively. The simulation domain ranges from close to the black hole to $\sim 10^5 r_g$. The initial magnetic field is again purely poloidal. Different from the first simulation, the magnetic field is broken into eight poloidal loops of alternating polarity. Each loop carries the same amount of magnetic flux, so that the black hole is unable

to acquire a large net flux over the course of the simulation. The simulation is performed using the HARM code. It is run for a time of $2 \times 10^5 GM/c^3$ and achieves inflow equilibrium (i.e., accretion has reached a steady state) out to a radius $\sim 90 r_g$. The readers are referred to Narayan et al. (2012) for details. By using the trajectory approach to study the wind properties using data from both simulations, we find that the main results are very similar. Therefore, in this paper, we choose to only focus on the latter simulation (3D GRMHD). Throughout this paper, we use the spherical coordinate. The physical quantities in the present paper, if not specified, are in units of $G = M = c = 1$.

2.2. Trajectory Method

Trajectory is related to the Lagrangian description of fluid, obtained by following the motion of fluid elements at consecutive times. Streamline is associated with the Euler description of fluid, obtained by connecting the velocity vectors of adjacent fluid elements at a given time. Trajectory is only equivalent to the streamline for strictly steady motion, which is not the case for accretion flow since it is always turbulent. Streamlines are easy to obtain and are widely used in the literature. On the other hand, obtaining Lagrangian trajectories is much more time-consuming than streamlines, but they loyally reflect the motion of fluid elements. For our purpose, we should consider trajectories rather than streamlines.

To get the trajectory, we first choose a set of “test particles” in the simulation domain within the outermost radius where inflow equilibrium is achieved, $\sim 90 r_g$, at a given snapshot at time t of the simulation. They are not real particles, but a collection of spatial coordinates as the starting point for the trajectory calculation. With their velocities interpolated from simulation data, we can then obtain their location at time $t + \delta t$. This process is then continued until the end of the simulation or when test particles leave the simulation domain. We use the “VISIT” software to perform particle trajectory calculation, which can do interpolation with a controlled precision. Obviously, to obtain robust particle trajectories, the time step of the simulation data output δt must be sufficiently small. This timescale depends on how fast the velocity of the particles changes during their motion, which is the Keplerian timescale. So the Keplerian timescale must be properly time-resolved. We have tested in our calculations using different time resolutions and compared the corresponding trajectory to see whether the results converge. If not, we shorten the time step of the simulation data output. The time step we actually use in obtaining the trajectory is roughly the Keplerian timescale at $r \approx 6 r_g$, which is much shorter than the Keplerian timescale of most of the region of the accretion flow. Taking 100 particles at various radii as an example, we have tested two time steps, with one being the Keplerian timescale at $6 r_g$ and another the Keplerian timescale at $4 r_g$. We found that the results such as the particle trajectories are largely indistinguishable.

3. RESULTS

Before describing our results, we first define some terminologies. We use “outflow” to describe any flow with a positive radial velocity v_r , i.e., flowing outward. This includes both “turbulent outflow” and “real outflow.” The difference between them is that in the former case the test particle will eventually return and join the accretion flow after flowing

outward for some distance, while in the latter case the test particle continues to flow outward and eventually escapes the outer boundary of the simulation domain.⁶ “Real outflow” consists of two components, i.e., disk jet and wind. Here, “disk jet” is different from the Blandford–Znajek jet in several aspects, as we have summarized in Yuan & Narayan (2014). Very briefly, “disk jet” originates from the innermost region of the accretion flow. It is quasi-relativistic and matter dominated. The Blandford–Znajek jet is powered by the spin of the black hole. It is relativistic and Poynting flux dominated. In the present paper, we do not have a Blandford–Znajek jet since the simulation data we use are for a Schwarzschild black hole. As we will describe in detail later, we find that the disk jet is confined in a region of $\theta \lesssim 15^\circ$ away from the polar axis while the wind is located between the jet boundary and the surface of the accretion flow. The velocity of the jet is much higher than that of the wind.

Note that the definition of wind we adopt here is different from that adopted in some literature (e.g., Narayan et al. 2012; Sadowski et al. 2013), where they require that the Bernoulli parameter of wind must satisfy $Be > 0$. The Bernoulli parameter of our wind can be of any value, negative or positive, at any radius. Our argument is that for non-steady accretion flow, Be is not constant along trajectories, but usually increases outward (refer to Figure 9). This means that even though $Be < 0$ at a certain radius, the wind particles can still escape to infinity. In fact, as we will describe later, we find that no matter what value Be is, the poloidal speed of wind does not decrease when they propagate outward until a radius within which turbulence is developed (refer to Figure 8 and relevant discussions later). In addition, technically the value of Be of wind should depend on the initial condition of the simulation because of energy conservation. In many simulations, including the current one, the initial condition is a bound torus and thus Be is negative. But in reality, the accretion flow comes from much farther away, so Be is more likely positive. This implies that the value of Be obtained in simulation should be regarded as a lower limit.

3.1. Overall Result: Confirmation of the Wind

Figure 1 shows the trajectories of sample test particles that originated from locations $(r, \phi) = (80 r_g, 0)$ and $\theta = 0 - \pi$. The left and right panels show the trajectories at the 3D and 2D ($r - \theta$ plane) space, respectively. The results are similar for test particles originating from different radii.

From the figure we clearly see that winds are evident. They are largely located in the polar region, i.e., $\theta \sim 0 - \pi/4$ and $\theta = 3/4\pi - \pi$, and are symmetric with respect to the equatorial plane. The trajectories of many test particles in this region are almost straight lines in the poloidal plane and $\theta \sim \text{const.}$, indicating that turbulence is weak. There are also many other more turbulent trajectories with varying θ values during outflowing motion. The specific angular momentum of wind particles is found to be larger than that of the inflow, consistent with Yuan et al. (2012a). The wind region almost overlaps with the usual “coronal” region above the main body of accretion flow (refer to Figure 4 in Yuan & Narayan 2014), and the

⁶ In some cases, e.g., if the initial radii of test particles are small, some particles could not escape beyond the outer boundary by the end of the simulation. On the other hand, they keep moving radially outward without any signs of return (the poloidal speed does not decrease outward; refer to Figure 8); we regard them as representing real outflow.

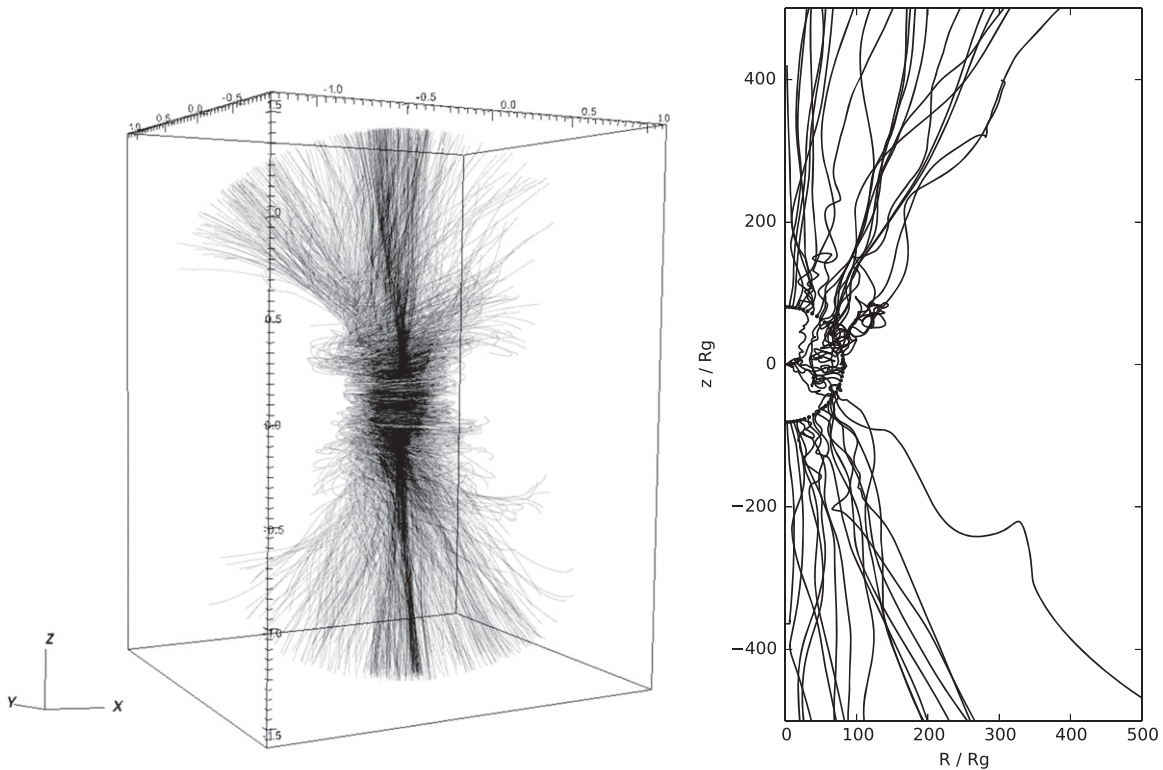


Figure 1. Lagrangian trajectories of the “test particles” originating from $r = 80 r_g$ (the black circle in the right panel) in the 3D space (left) and 2D $(r - \theta)$ plane (right). Real outflows are evident in the coronal region. The inflow concentrates within the main disk body around the equatorial plane, and their motion is more turbulent.

boundary of the wind region is about the surface of the accretion flow defined by the density scale height. In other words, the disk corona is outflowing. The main disk body, i.e., $\theta = \pi/4 - 3/4\pi$, is the “inflow” region. Most of the test particles originating from this region move inward, and their motion is turbulent. This turbulent motion is due to the magnetorotational instability (MRI; Balbus & Hawley 1998), as usual. Interestingly, we also find that some test particles originating from this region first move vertically toward the coronal region and then escape outward radially as disk wind. Such vertical motion is present in almost any radius and is perhaps an indicator of the magnetic buoyancy. This supplies new gas from the disk body to the corona/wind. Overall, the structure of the accretion flow is that the inflow region corresponds to the main disk body, while the wind region corresponds to the disk corona. This picture is consistent with Sadowski et al. (2013; see their Figure 16).

3.2. The Mass Flux of Outflow and Inflow

To calculate the mass flux of the inflow and outflow, and to analyze the wind properties, we distinguish between various types of particle trajectories. In Figure 2, we show characteristic types of characteristic particle trajectories originating from radius r . Distinguishing them is crucial for calculating the mass fluxes of the inflow and outflow correctly, as well as analyzing the wind properties.

1. The red and black lines represent outflows and inflows, respectively.
2. The red solid line represents a real outflow, where the particle keeps moving outward and never crosses the radius r during its motion.

3. The red dashed and red dotted lines represent turbulent outflows, where the particles first move outward but will later return and cross the radius r during their motion. Although the particles eventually move outward and inward, they both belong to the “turbulent outflow” category when we calculate the mass flux.
4. It is similar for the three black lines except that they all represent inflow. The solid line represents real inflow, while both the dashed and dotted lines represent turbulent inflow.

To calculate the mass flux (or mass flow rate) of the wind $\dot{M}_{\text{wind}}(r)$ at a given time, we first choose test particles initially distributed at fixed radius r with different θ and ϕ and obtain their trajectories. The “real outflow rate” is then calculated by summing up the corresponding mass flux carried by test particles whose trajectories belong to the real outflow (the red solid line in Figure 2)

$$\dot{M}_{\text{wind}}(r) = \sum_i \rho_i(r) v_{r,i}(r) r^2 \sin(\theta) \delta\theta_i \delta\phi_i. \quad (4)$$

Here $\rho_i(r)$ and $v_{r,i}$ are the mass density and radial velocity at the location where test particle “ i ” originates, and $\delta\theta_i$ and $\delta\phi_i$ are the ranges of θ and ϕ the particles occupy. We can obtain the “real inflow rate” with a similar approach. In this case, we sum up the corresponding mass flux of test particles whose trajectories are analogous to the black solid line in Figure 2. The mass flux corresponding to the dotted and dashed red lines is the “turbulent outflow rate,” while that corresponding to the dashed and dotted black lines is the “turbulent inflow rate.”

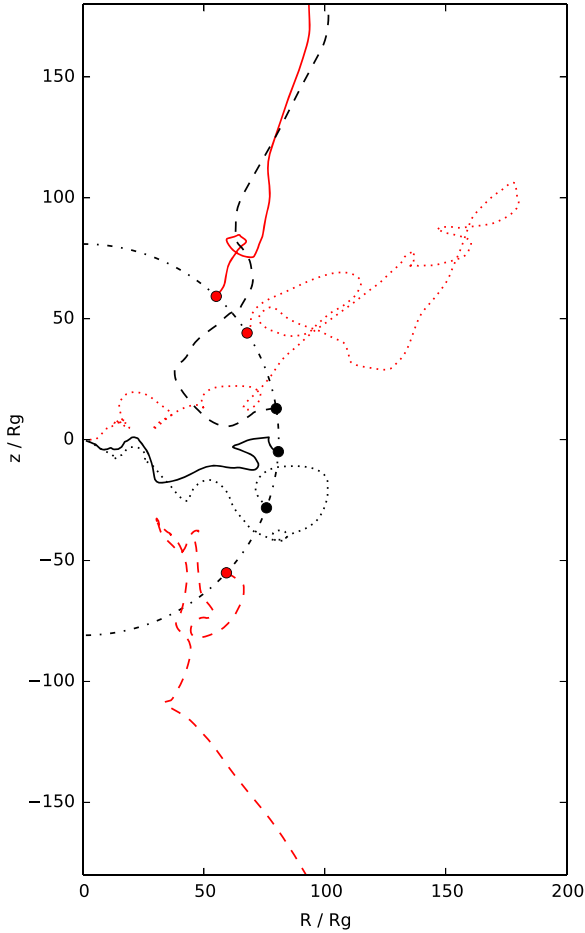


Figure 2. Various types of trajectory of “test particles” in the accretion flow. Red lines denote outflow, while black ones are for inflow. See Section 3.2 for details.

Figure 3 shows the mass flow rate at $r = 80 r_g$ per unit θ and ϕ as a function of θ . The left panel shows the mass flux at two different times but the same ϕ , while the right panel shows the mass flux at two different ϕ but the same time. A positive value is for real outflow, while a negative value is for total inflow, i.e., including both the “real inflow” and “turbulent inflow.” By comparing the black and red lines in the left and right panels, we see that the specific values of θ at which real outflows reside change with ϕ and time. In other words, for a fixed θ , the flow can be inflow or outflow for different time t and ϕ .⁷ This result indicates that if we move the $t\phi$ average inside the integrals of Equation (2), i.e., to integrate $\max(\langle \rho v_r \rangle_{t\phi}, 0)$ as in Narayan et al. (2012), significant mass flux of the real outflow will be canceled and we will substantially underestimate the mass flux of the real outflow. This is the main reason why Narayan et al. (2012) reported much weaker real outflow than Yuan et al. (2012a). This also explains why Narayan et al. (2012) reported that the mass flux of the real outflow does not converge with time since more mass flux will be canceled if the period of integration time is longer. Figure 4 shows the mass flow rate integrated over all ϕ and averaged from time $t = 100,000$ to $120,000 M$ at radius $r = 80 r_g$ as a function of θ . As with

⁷ The values of time in the left panel and the values of ϕ in the right panel are chosen so that the change of inflow and outflow for a fixed θ is significant.

Figure 3, positive and negative values are for real outflow and total inflow, respectively.

From Figures 3 and 4 we see that, consistent with the qualitative result shown in Figure 1, the inflow primarily takes place in the main disk body, while most of the mass flux of the real outflow occurs in the range of $\theta = 30^\circ - 60^\circ$. But as we have pointed out in Section 3.1, for some values of ϕ at any radius, some real outflow also exists in the main disk body. This can be seen from Figure 4, which shows some significant mass flux of the real outflow even close to the equatorial plane, i.e., $\theta \sim 100^\circ$. We hardly see this wind in Figure 1 because these wind particles first quickly move vertically to the surface of the accretion flow before moving outward as outflowing wind.

The next important questions are, what is the mass flux of the real outflow, and how does it compare with the total outflow rate calculated by Equation (2)? By integrating the wind mass flux shown in Figure 4 over θ but without doing the time average, we can obtain the total real outflow rate at a given time and radius. Then we can obtain the radial profile of mass flux of the real outflow. The red dashed line in Figure 5 shows the result at $t = 100,000 M$.⁸ We find that the radial profile of the mass flux of wind can be well described by

$$\dot{M}_{\text{wind}}(r) \approx \dot{M}_{\text{BH}} \left(\frac{r}{40 r_g} \right)^s \equiv \dot{M}_{\text{BH}} \left(\frac{r}{20 r_s} \right)^s, \quad s \approx 1, \quad (5)$$

where \dot{M}_{BH} is the mass accretion rate at the black hole horizon. So the mass flux of the wind at $40 r_g$ is equal to the mass accretion rate to the black hole \dot{M}_{BH} . Such a power-law distribution is likely valid up to the outer boundary of the accretion flow and then quickly decreases beyond the outer boundary (F. Yuan et al. 2015, in preparation). For comparison, we have also shown in the figure by the red and black solid lines the total outflow and total inflow rates calculated by Equations (1) and (2), and the mass flux of the real outflow calculated following the method in Narayan et al. (2012) by the red dotted line. We can see that the mass flux calculated by Equation (2) is equal to \dot{M}_{BH} at $30 r_g$, while that calculated by the Narayan et al. (2012) method is much weaker, equal to \dot{M}_{BH} at $100 r_g$. Sadowski et al. (2013) adopted the same method as Narayan et al. (2012) to study the mass flux of the real outflow but could not obtain a radial profile, because they found that the mass flux of the real outflow is too weak and thus difficult to fit using any formula. We also note that the power-law index in Equation (5) is in good agreement with that obtained from the analytical study by Begelman (2012).

Also shown in the figure by the red dot-dashed line is the mass flux of the disk jet. We find that when $r \lesssim 400 r_g$, the mass flux of the disk jet can be described by

$$\dot{M}_{\text{jet}}(r) = \frac{1}{20} \dot{M}_{\text{wind}}(r). \quad (6)$$

The mass flux increases with radius, indicating that the jet is gradually supplied by matter from the wind. When $r \gtrsim 400 r_g$,

⁸ We want to point out a caveat here. As we have stated in Section 2.1, the inflow equilibrium is reached only up to $\sim 90 r_g$ in our simulation, but the x-axis of the figure extends to $200 r_g$.

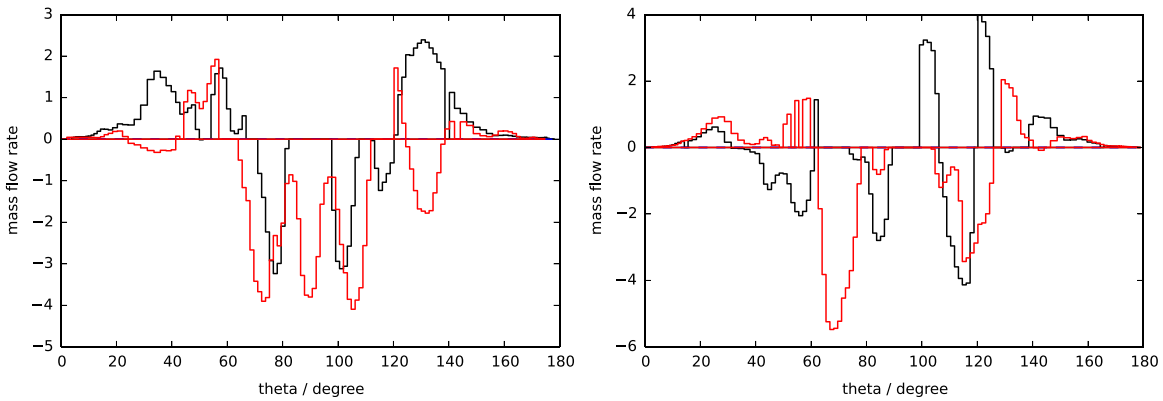


Figure 3. Mass flux per unit θ and ϕ at $r = 80 r_g$ as a function of θ . Left: black and red lines are for $t = 104,000$ and $120,000 M$, respectively, at fixed $\phi = 0$; Right: black and red lines are for $\phi = 5\pi/4$ and $3\pi/2$, respectively, but fixed time $t = 100,000 M$. A positive value corresponds to real outflow, while a negative value corresponds to total inflow (i.e., including turbulent inflow).

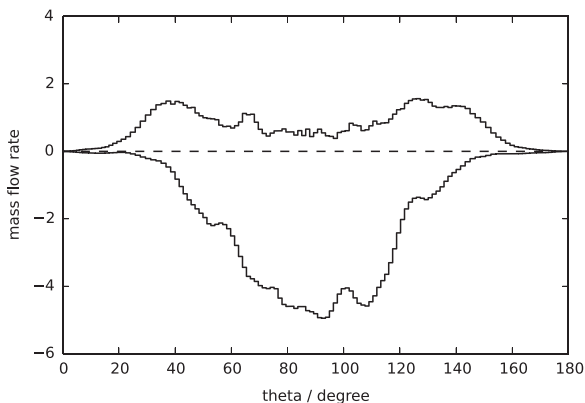


Figure 4. Mass flux per unit θ but integrated over all ϕ and averaged from time $t = 100,000$ to $120,000 M$ as a function of θ at radius $r = 80 r_g$. The positive and negative values are for the real outflow and total inflow, respectively. Note that significant mass flux of wind is also produced from the disk body, i.e., around $\theta \sim 100^\circ$. These wind particles first move vertically toward the disk surface and then escape outward from there.

however, the mass flux of the jet is found to be almost saturated.

3.3. The Poloidal Speed

In this subsection, we consider the evolution of poloidal velocity in the wind. This is the dominant component of the wind velocity at large disk radii once magnetic field becomes subdominant. Figure 6 shows the poloidal speed of the real outflow as a function of θ for various ϕ at three different radii, $r = 40, 80,$ and $160 r_g$, and $t = 100,000 M$. To obtain these three plots, we first choose some test particles at various θ and ϕ at the three radii and obtain their trajectories. We then select those particles corresponding to real outflow and obtain their poloidal speed. We can see that the poloidal speed as a function of θ has a sharp jump at $\theta \sim 15^\circ$ away from the rotation axis. The poloidal speed of outflow close to the axis is $\gtrsim 0.3 c$, much larger than that away from the axis, which is $\lesssim 0.05 c$. We thus can naturally identify the real outflow within $\theta \sim 15^\circ$ to the axis as the “disk jet,” while the real outflow out of this range is wind. Note that the simulation data we use are for a non-rotating black hole, so the presence of the disk jet is irrelevant to black hole spin, although the spin of the black hole may strengthen the disk jet (e.g., Sadowski et al. 2013). The disk jet

originates from the inner disk region and is powered by the rotation energy of the accretion flow. This is different from the Blandford–Znajek jet originating from the black hole horizon (Blandford & Znajek 1977), which is powered by the black hole spin energy. Other differences between the two types of jet include that the disk jet is sub-relativistic and matter dominated, while the Blandford–Znajek jet is relativistic and Poynting flux dominated (see Yuan & Narayan 2014 for a summary).

By comparing the three plots in Figure 6, we see that the poloidal wind velocity seems to decrease with increasing radius. To quantify, we calculate the mass-flux-weighted poloidal speed of the real outflow as a function of radius. We distinguish the two types of the real outflow, i.e., wind and disk jet, in our calculations. For this purpose, when calculating the poloidal wind velocity, the integration is only over the range of $15^\circ \lesssim \theta \lesssim 165^\circ$, while for the entire outflow, we integrate over all θ . The results are shown by blue (total outflow) and red (wind only) dots in Figure 7. The poloidal velocity of the total outflow is slightly higher than that of wind, as expected. The lines are fitting functions, approximately given by

$$v_{p,\text{wind}}(r) \approx 0.21 v_k(r). \quad (7)$$

Here $v_k(r) (\equiv (GM/r)^{1/2})$ is the Keplerian speed at radius r . We note that this equation describes the poloidal velocity of wind at radius r . On the one hand, the wind can be launched from any radius $\lesssim r$. On the other hand, we see in Figure 5 that the wind mass flux increases rapidly with radius. Therefore, the mass-flux-weighted wind velocity (Equation (7)) primarily reflects wind launched close to radius r .

We have also calculated the evolution of the poloidal wind velocity along individual test particle trajectories. The results are shown in Figure 8. In the left panel, six representative test particles are shown, initially located at $r = 80 r_g$ but different θ . Specifically, the red dot-dashed line corresponds to $\theta = 10^\circ$, i.e., within the disk jet region, while others have $\theta \gtrsim 20^\circ$. The three red lines have a positive Bernoulli parameter at $80 r_g$, while the three blue lines have $Be < 0$ at $80 r_g$ (refer to Figure 9). The acceleration of the red dot-dashed line is the most significant, indicating strong acceleration in the jet region. This is confirmed by our detailed analysis of the acceleration mechanism in Section 4. We see that the blue dashed and red solid lines in the left panel of the figure also show strong

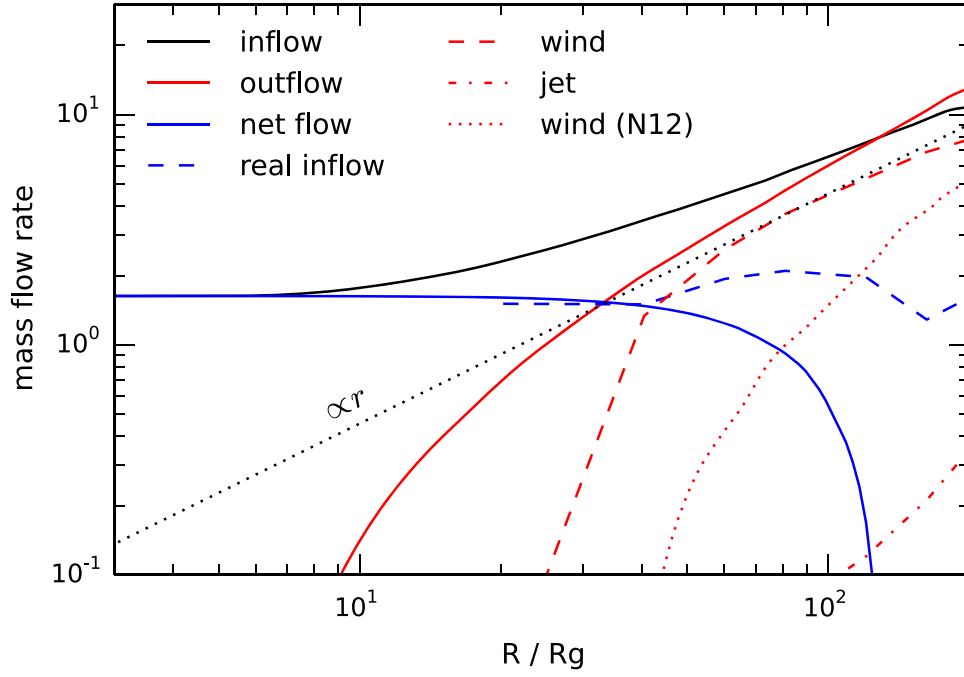


Figure 5. Various mass flow rates as a function of radius. Black and red solid lines show the total inflow and outflow rates, respectively, calculated following Equations (1)–(2), while the blue solid line denotes their difference. The red and blue dashed lines denote the mass flux of the real outflow and real inflow calculated at $t = 100,000 M$, respectively. The red dot–dashed line shows the mass flux of the disk jet. For comparison, we also show by the red dotted line the mass flux of the real outflow calculated following the method in Narayan et al. (2012).

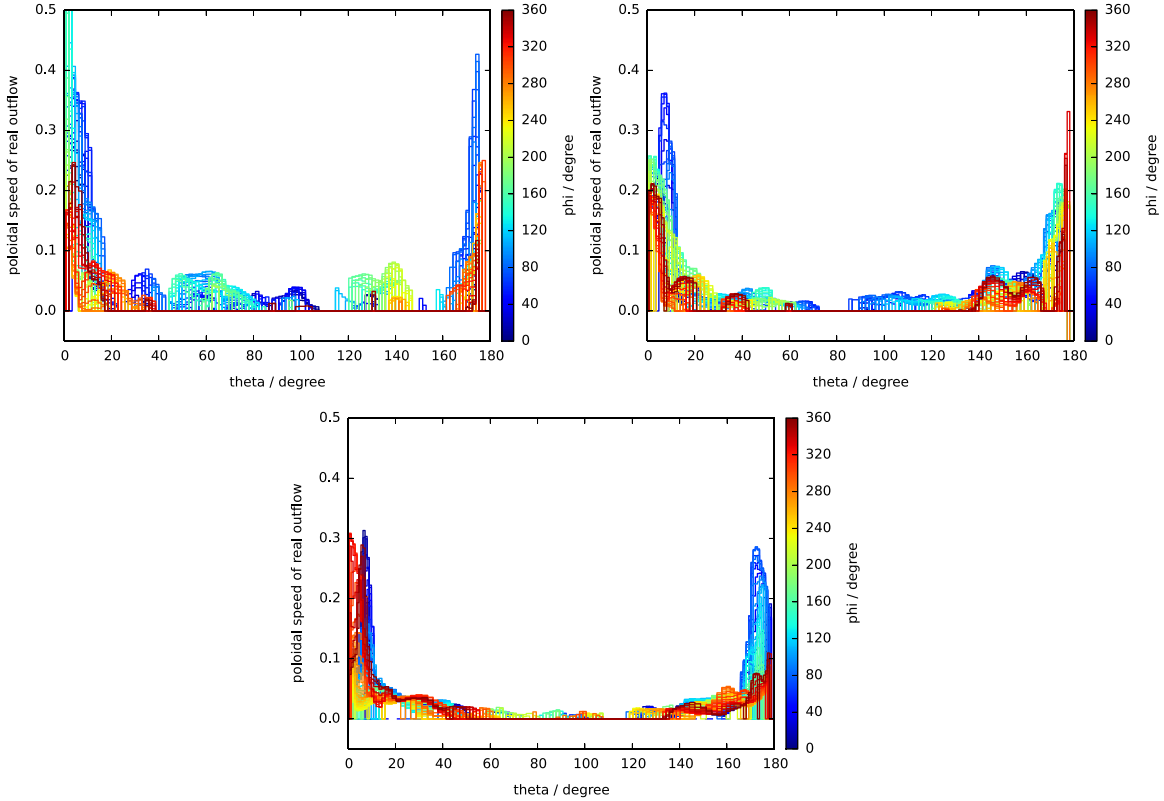


Figure 6. Poloidal speed in units of speed of light of real outflow as a function of θ for $r = 40 r_g$ (top left), $80 r_g$ (top right), $160 r_g$ (bottom) and various ϕ at $t = 100,000 M$. The values of ϕ are denoted by the color of the lines. We can see that close to the axis, $\theta \lesssim 10^\circ$ and $\theta \gtrsim 170^\circ$, the poloidal speed is much larger than in other regions. We identify this as part of the outflow jet.

acceleration. This is likely because these two test particles later enter the “jet region” although they are initially located out of this region. In fact, we find that the θ values of many test

particles change significantly as they travel outward. For other lines (particles always in the wind region), while there are fluctuations, the poloidal wind velocity roughly remains

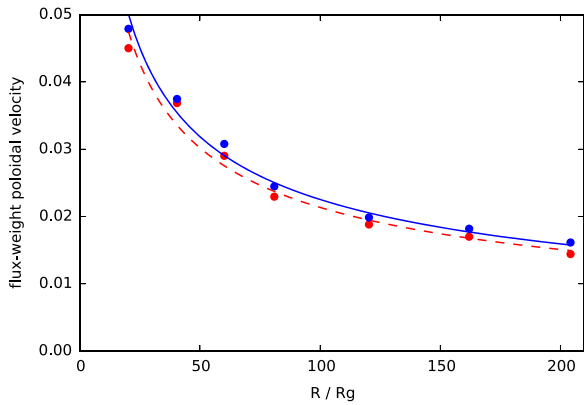


Figure 7. Mass-flux-weighted poloidal speed in units of speed of light at $t = 100,000 M$. The blue and red lines correspond to total outflow (i.e., averaged for all θ) and wind (i.e., averaged over $15^\circ \lesssim \theta \lesssim 165^\circ$), respectively.

constant along the particle trajectories, extending from $r = 80 r_g$ to $r \sim 800 r_g$, regardless of the sign of their initial Be . Beyond $r \sim 800 r_g$, the poloidal velocity seems to decrease with radius. This is related to the value of Be . We will argue in the next subsection that such a decrease is likely not reliable.

In the right panel of Figure 8, we show the averaged poloidal velocity of eight test particles along their trajectories. The initial locations of these particles are uniformly distributed in θ . The red and black lines correspond to particles originating from $r = 40 r_g$ and $160 r_g$, respectively. The initial poloidal velocities of the red lines are larger than those of the black lines, consistent with Figure 7. We further distinguish the dashed lines, which correspond to particles that are *initially* located in the wind region ($15^\circ \lesssim \theta \lesssim 165^\circ$), and the solid lines, corresponding to particles that *always* stay in the wind region along their trajectories. We see that the particle poloidal velocity either remains constant or slightly increases outward along the trajectory. Solid and dashed lines differ significantly because we are not using the mass-flux-weighted average. The increasing or constant behavior of the poloidal velocity with radius strongly suggests that additional acceleration forces must operate to compensate for the change in gravitational energy, which will be discussed in Section 4.

From Figure 8, we deduce that the asymptotic terminal poloidal wind velocity originating from radius r can be approximated by

$$v_{p,\text{term}}(r) \approx (0.2 \sim 0.4)v_k(r). \quad (8)$$

Note the different meaning between this equation and Equation (7). This result also compliments the discussion following Equation (7): the measured wind at any given radius, say, r , is a mixture of wind launched from smaller disk radii and wind that is produced more locally. The former typically has higher velocity but carries smaller mass flux, while the latter carries higher mass flux with smaller velocity. Overall, Equations (7) and (8) are approximately consistent with each other, and they are also consistent with values estimated in Yuan et al. (2012a; Section 3.5).

3.4. The Bernoulli Parameter of the Real Outflow

We now discuss the Bernoulli parameter of the wind. Following Penna et al. (2013a), we adopt in the present paper

the following definition of the Bernoulli parameter with the magnetic term included:

$$Be = -\frac{\rho u_t + \Gamma u u_t + b^2 u_t}{\rho} - 1, \quad (9)$$

where $\Gamma = 5/3$ is the adiabatic index, u_t is the time component of the four-velocity, u is the internal energy, and b is magnetic field strength in the fluid frame. The rest mass energy is subtracted. Far from the black hole, the above equation reduces to the Newtonian quantity, i.e., the sum of kinetic energy, gas enthalpy, and magnetic enthalpy.

The evolution of the Bernoulli parameter along the trajectories of representative wind particles is shown in Figure 9. The three red lines have a positive Be at the starting point, while the three blue lines have a negative initial value of Be . From this figure, we find the following results.

First, the value of Be is not a constant along particle trajectories. This is not unexpected because conservation of Be holds only when the accretion flow is strictly steady and inviscid, while real accretion flow is always turbulent. As a result, it is inappropriate to use the sign of Be to judge whether the flow can escape to infinity, especially when the outflow is still within the radius at which turbulence is well developed.

Second, for outflow originating from smaller θ , Be increases to very large values at large radii. On the other hand, the value of Be varies much less significantly and roughly remains constant for the wind originating from closer to the disk surface. Comparing with Figure 8, we see that changes in Be correlate positively with changes in poloidal velocity. For the three trajectories whose Be increases outward, there is also significant acceleration in their poloidal velocities. This is because their θ values gradually decrease and enter into the jet region, thus experiencing strong acceleration.

It is interesting to note that for wind originating within $40^\circ \lesssim \theta \lesssim 50^\circ$, their value of Be becomes almost constant when $r \gtrsim 800 r_g$. This corresponds to the slight decrease of the poloidal velocity beyond $\sim 800 r_g$ shown in the left panel of Figure 8. The reason why Be does not change beyond $800 r_g$ is because in this region turbulence has not well developed within our simulation time. Note that this radius is different from the inflow equilibrium radius, which is $\sim 90 r_g$. Within $\sim 90 r_g$, everything, especially the radial density profile, is fully reliable. Beyond this radius, the density profile is not reliable, but other properties, such as the level of turbulence and subsequently outflow properties, are still reliable up to a much larger “turbulence radius,” the limiting radius of turbulence steady state. This radius can be estimated as follows. Turbulence in accretion flow is because of MRI. The fastest growth rate of MRI at radius r is $\sim \Omega(r)$. More precisely, it takes 3–4 orbits for MRI to develop and ~ 10 orbits to saturate (Hawley et al. 1995). For our simulation time of $t_{\text{simulation}} \sim 2 \times 10^5$, taking a timescale of 3 orbits, we can obtain that the “turbulence radius” is $\sim 500 r_g$. This is close to the value of $800 r_g$ mentioned above. Another way to understand the “turbulence radius” is as follows. For a geometrically thick disk, the largest turbulence eddies have size of order r . The corresponding eddy turnover time is $r/\sigma(r)$, where $\sigma(r)$ is the rms turbulent velocity. Our simulation data show $\sigma(r) \sim 0.15v_k(r)$. If at a certain radius the eddy turnover time is substantially smaller than the duration of the simulation, then the local turbulence is likely to have reached quasi-steady state.

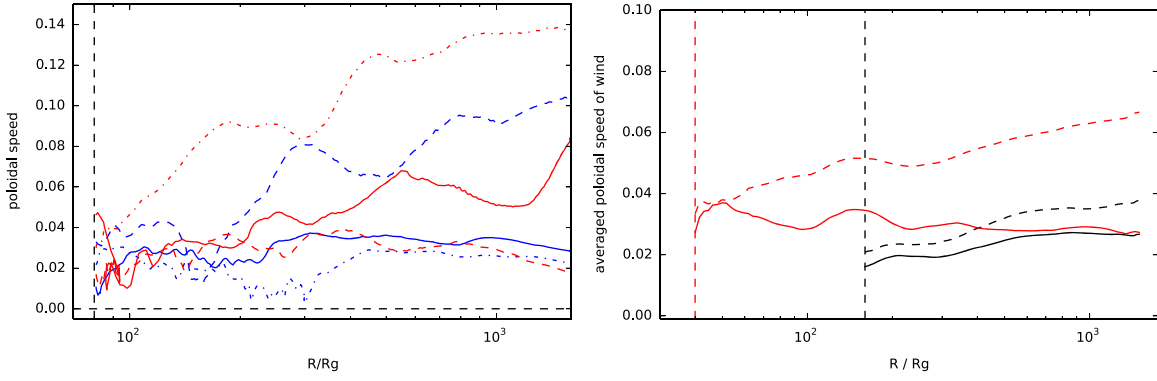


Figure 8. Left: evolution of the poloidal velocity of real outflows along test particle trajectories (originated from $r = 80 r_g$). The three red lines have $initial Be > 0$, while the three blue lines have $initial Be < 0$. The exact values of Be along the trajectories can be found from Figure 9. From top to bottom, the red dot-dashed, blue dashed, and red solid lines correspond to particles originating from $\theta \sim 10^\circ, 20^\circ, 30^\circ$, respectively. The red dashed, blue solid, and blue dot-dashed lines correspond to $\theta \sim 40^\circ \lesssim \theta \lesssim 50^\circ$. Right: spatially averaged poloidal velocity of real outflows originating from $40 r_g$ (red lines) and $160 r_g$ (black lines) along their trajectories. The dashed lines are calculated from wind particles originating from the region of $15^\circ \lesssim \theta \lesssim 165^\circ$, while the solid lines are calculated from wind particles always satisfying $15^\circ \lesssim \theta \lesssim 165^\circ$ in their trajectories.

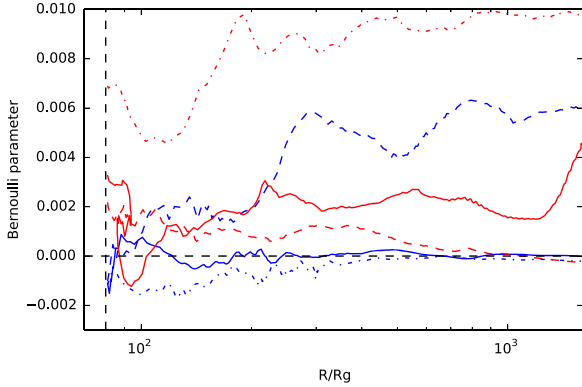


Figure 9. Same as the left panel of Figure 8, but for the Bernoulli parameter Be .

Therefore, the “turbulence radius” should be some fraction of $\sigma(r)t_{\text{simulation}}$, which gives a similar result to the above estimation. Therefore, we think that the results beyond $\sim 800 r_g$ are not reliable. It is very likely that Be will keep changing and the poloidal velocity still remains constant beyond $800 r_g$. This implies that wind can at least escape beyond the outer boundary of accretion flows. Simulations with longer run times can check this point.

Although Be is not a constant along particle trajectories, it is still useful to decompose Be into individual physical terms and compare their contributions, as shown in Figure 10. The left and right panels correspond to particles originating from jet and wind regions, respectively. In the case of the disk jet, it is mainly the enthalpy that compensates for the increase of gravitational energy and kinetic energy. Magnetic energy also plays an active role at smaller radius ($r \lesssim 100 r_g$). In the case of wind, the role of magnetic energy appears unimportant. The increase of gravitational energy is mainly compensated by the reduction of specific enthalpy and kinetic energy. But we note that although the total kinetic energy decreases along the trajectory, the poloidal component does not. It usually keeps constant, as shown by Figure 8. This corresponds to the work done by the centrifugal force, as we will discuss in Section 4.

3.5. The Fluxes of Energy and Momentum of Wind and Jet

Based on the trajectory analysis, we now calculate the energy and momentum fluxes from both the wind and jet as follows:

$$\dot{E}_{\text{jet(wind)}}(r) = \int \frac{1}{2} \rho(r, \theta, \phi) v_p^3(r, \theta, \phi) r^2 \sin(\theta) d\theta d\phi, \quad (10)$$

$$\dot{P}_{\text{jet(wind)}}(r) = \int \rho(r, \theta, \phi) v_p^2(r, \theta, \phi) r^2 \sin(\theta) d\theta d\phi. \quad (11)$$

Here $v_p(r)$ is the poloidal velocity at radius r , for which we assume $v_p(r) \approx v_r(r)$ in our calculation because we find $v_\theta \ll v_r$. The integration over θ for wind and the disk jet is bounded by $\theta \approx 15^\circ$, according to Figure 6.

Figures 11 and 12 show the radial profiles of energy and momentum fluxes, respectively, calculated at $T = 100,000 M$. In both figures, the red solid and blue dashed lines are for the wind and disk jet, respectively. We see that the energy flux of the wind is $\gtrsim 3$ times stronger than that of the disk jet, while the contrast in the momentum flux between wind and jet is much larger. This is again mainly because of the low density in the disk jet. From Figure 11, we see that the energy flux of the wind rapidly increases at small radii and then becomes almost saturated at $r \gtrsim 40 r_g$. The rapid increase corresponds to the rapid increase of the wind mass flux with radius when $r \lesssim 40 r_g$ (see Figure 5). For $r \gtrsim 40 r_g$, we have

$$\dot{E}_{\text{wind}}(r) \approx \frac{1}{2} \dot{M}_{\text{wind}}(r) v_{p,\text{wind}}^2(r) \approx \frac{1}{1000} \dot{M}_{\text{BH}} c^2. \quad (12)$$

In the above calculation, Equations (5) and (7) are used. This result indicates that the energy flux at large radius is roughly saturated, consistent with Figure 11. The main reason energy flux saturates is $s = 1$ in Equation (5). For the momentum flux of the wind, we have

$$\dot{P}_{\text{wind}}(r) \approx \dot{M}_{\text{wind}}(r) v_{p,\text{wind}}(r) \propto r^{1/2}. \quad (13)$$

This is consistent with the result shown in Figure 12.

The energy flux obtained in Equation (12) is in good agreement with that required in large-scale AGN feedback simulations (e.g., Ciotti et al. 2010; Gaspari et al. 2012). In these works, AGN feedback is involved to heat the intercluster

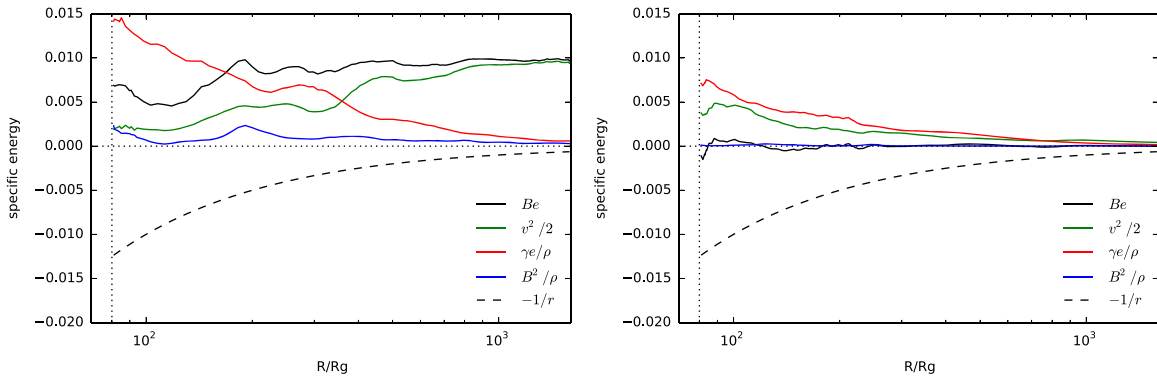


Figure 10. Decomposition of the Bernoulli parameter (black solid) into individual contributions along Lagrangian test particle trajectories for the disk jet (left) and wind (right). Individual terms include gravitational energy ($\propto 1/r$; black dashed), specific kinetic energy ($\propto v^2/2$; green), specific enthalpy ($\gamma e/\rho$; red), and specific magnetic energy (B^2/ρ ; blue). The test particles are initially located at $R = 80 r_g$, starting at $t = 100,000 M$.

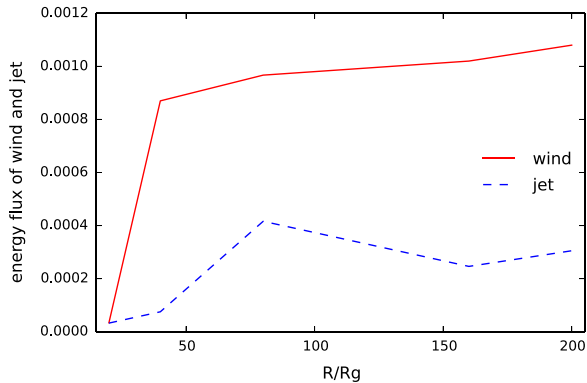


Figure 11. Radial profile of the energy fluxes of the wind (red solid) and jet (blue dashed).

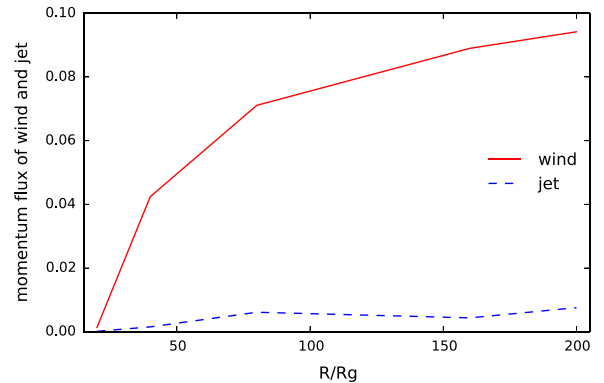


Figure 12. Radial profile of the poloidal momentum fluxes of the wind (red solid) and jet (blue dashed).

medium to compensate for the rapid cooling rate in the systems (i.e., the cooling flow problem). It was found that to be consistent with observations of both isolated galaxies and galaxy clusters, the required “mechanical feedback efficiency,” defined as $\epsilon \equiv \dot{E}_{\text{wind}}/\dot{M}_{\text{BH}}c^2$, must be in the range of $\sim 10^{-3} - 10^{-4}$. Our results provide a natural explanation for the required value of ϵ , at least when the AGN is in the hot accretion mode.

Our results highlight the importance of wind over jet on AGN feedback. On the other hand, one important caveat is that our calculation is based on the simulation of a Schwarzschild black hole. If the black hole is rapidly spinning, the power of the disk jet is expected to become stronger (Sadowski et al. 2013). In addition to the disk jet, a Poynting-flux-dominated jet (BZ jet) will be produced through the black hole horizon, powered by the black hole spin (Blandford & Znajek 1977; Komissarov 2001; McKinney 2005; Hawley & Krolik 2006; Tchekhovskoy et al. 2010, 2011; Penna et al. 2013b). The dependence of the power of the BZ jet on spin is clear (see references above), while the dependence of the disk jet and wind on spin remains to be investigated, perhaps less sensitive compared to the BZ jet.

In addition to the black hole spin, another parameter is the magnetic flux threading the inner region of the accretion flow. In our simulation, this flux is small and the accretion flow is called to be in the “SANE” state (Narayan et al. 2012). If the flux is large, the system enters the “magnetically arrested disk” (MAD) state. There have been some studies on the dependence of the jet and wind power on the magnetic flux. For example, it

has been found that in the MAD state, the power of the BZ jet will dominate the disk jet (Narayan et al. 2003; Tchekhovskoy et al. 2010; Penna et al. 2013a; see review by Yuan & Narayan 2014). Sadowski et al. (2013) compared the power of the wind and the jet and found that, if the black hole spin and magnetic flux at the horizon are large, jet power will usually dominate the wind power. But note that as we have described in the previous section, their estimation of the mass flux of wind should be regarded as a lower limit. For a rapidly spinning black hole accreting in the MAD limit, the power of the jet is even larger than the accretion power (Tchekhovskoy et al. 2011, 2012). A systematic study on the dependence of the jet and wind power on magnetic flux and black hole spin is required. We plan to revisit this problem in the next work.

4. THE MECHANISM OF PRODUCING OUTFLOW

4.1. Mechanism of the Acceleration of Wind

To study the production and acceleration mechanism of the wind and jet, we have calculated the forces at the jet and wind region at a single point and a given snapshot. The locations where we evaluate the forces correspond to real outflow based on our particle trajectory study. We note that forces are stochastic, but we found that our analysis can be regarded as representative, except in the cases we will mention below. Since we evaluate the forces in the frame co-rotating with the flow at the “evaluation location,” we should also include the centrifugal force, in addition to the gravitational force, gas

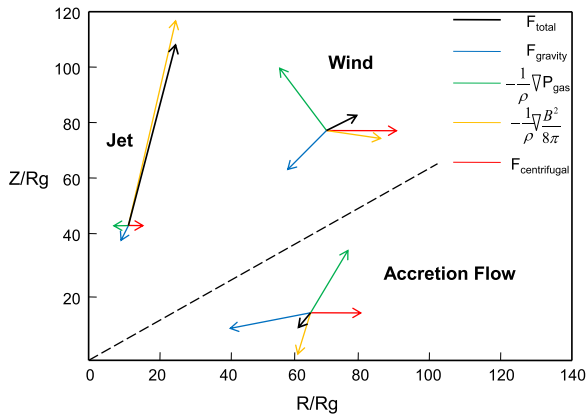


Figure 13. Force analysis at three representative locations corresponding to the disk jet, wind, and the main body of the accretion disk. The arrows indicate force direction, whose length represents force magnitude.

pressure gradient, and Lorentz force.⁹ We show the results for three representative points in the disk jet, wind, and main disk regions in Figure 13. For the wind, the main driving forces are the centrifugal force and magnetic pressure gradient. From the figure we notice that the gradient of the magnetic pressure is “downward,” pointing toward the positive θ direction. This is somewhat surprising because we usually expect that magnetic field becomes weaker away from the main disk body toward the coronal region. This reflects the strong fluctuation of the accretion flow. In fact, if we choose another time or another location to do the force analysis, we very likely find that the gradient of the magnetic pressure becomes “upward.” For the same reason, the direction of the gas pressure gradient also strongly fluctuates with time and location. But statistically, the gradients of both the gas and magnetic pressure are pointing along the positive r direction and thus are helpful to the acceleration of wind. Their magnitudes are also comparable to the centrifugal force, as shown by Figure 13.

From the figure we can see that the magnitude of the centrifugal force is larger than (or at least comparable to in general) the gravitational force. This means that the specific angular momentum of the wind is larger than or close to the Keplerian value. For comparison, we also show in the figure the force analysis in the inflow region. We see that the magnitude of the centrifugal force is now smaller than the gravitational force.¹⁰ This is consistent with the result obtained in Yuan et al. (2012a) that the specific angular momentum of the outflow is systematically larger than that of the inflow. This implies that some angular momentum is transferred from some fluid element to another, likely by the magnetic field lines from the main disk body to the coronal region. Once the combination of the centrifugal force and the pressure gradient exceeds the gravitational force, wind will be accelerated.

According to the above analysis, the mechanism of the acceleration of wind is similar to the Blandford & Payne (1982) mechanism in the sense that the centrifugal force plays an important role. The differences are that the gradient of the pressure plays a comparable role compared with the centrifugal force. In addition, there is no large-scale magnetic field formed in our simulation, and the wind region is not force-free.

⁹ We only include the gradient of magnetic pressure. Since $B_r \ll B_\phi$, the magnetic tension force is much weaker than the gradient of magnetic pressure, so we neglect the tension force.

¹⁰ This confirms that the accretion flow is sub-Keplerian.

4.2. Mechanism of the Acceleration of the Jet

In the case of the disk jet, the acceleration mechanism is completely different from that of Blandford & Payne (1982). Here the dominant force is the gradient of the toroidal magnetic pressure, consistent with the result of Hawley & Krolik (2006). This mechanism is the so-called magnetic tower mechanism (Lynden-Bell 2003; see also Shibata & Uchida 1985; Kato et al. 2004). The reason for the much higher jet velocity compared with the wind velocity is related to the strong magnetic field and low density. In the case of both the wind and jet, the energy of the outflow mainly comes from the rotation energy of the accretion flow. The rotation energy is converted into the magnetic energy, which then is converted into the kinetic energy of the wind and jet.

5. SUMMARY

Previous numerical simulations of the black hole accretion flow have shown that the mass accretion rate decreases inward (Equation (3)). It has been proposed that this may be caused by convection or outflow. Stability analysis, however, has indicated that the accretion flow is convectively stable when the magnetic field is present. This excludes the possibility of convective instability and leaves only the mass loss via outflow as the likely reason. However, previous theoretical works have obtained quite different results on the strength of outflow. In terms of the mass accretion rate onto the black hole horizon \dot{M}_{BH} , Narayan et al. (2012) found that even at $r \approx 90 r_g$, the mass flux of the real outflow is still very weak. On the other hand, Yuan et al. (2012a) argue that the mass flux of outflow should be strong, i.e., a significant fraction of that described by Equation (2).

One of the main aims of the present work therefore is to investigate how strong the real outflow is. It is well known that accretion flow is turbulent, so there must be some gas moving outward in any snapshot as part of turbulent eddies. These “turbulent outflows” are not “real outflows” since they will turn back and join the accretion flow. The main difficulty of obtaining the mass flux of the real outflow is therefore how to exclude the “contamination” of turbulent outflow in Equation (2). For this aim, instead of Equation (2), Narayan et al. (2012) move the $t\phi$ average inside the integral in Equation (2).

We have adopted a different approach to investigate this problem. We use a “trajectory approach” to analyze the data of GRMHD numerical simulations of accretion flow. Different from the streamline analysis often adopted in accretion flow study, this approach can provide the trajectory of each “virtual test particle” in the accretion flow and thus directly show whether the flow is turbulent outflow or real outflow. The most important result of our analysis is that the mass flux of the real outflow is found to be as high as $\dot{M}_{\text{wind}} \approx \dot{M}_{\text{BH}}(r/40 r_g)$ (i.e., Equation (5); refer to Figure 5). In other words, the mass flux of the real outflow is equal to \dot{M}_{BH} at $40 r_g$. As a comparison, the mass flux calculated by Equation (2) is equal to \dot{M}_{BH} at $30 r_g$. The reason why Narayan et al. (2012) found a much weaker outflow is that the real outflow is instantaneous. They wander around in 3D space, as shown by Figure 3, and thus will be canceled if the time average is done first.

Several other important results are as follows.

1. Most of the real outflow occurs in the coronal region of the accretion flow. Within the disk body, it is mainly inflow (Figure 1).

2. There are two distinct types of real outflow. One is within the region of $\theta \lesssim 15^\circ$ away from the axis, and another is outside of this region. In the former region, the poloidal speed of outflow is as high as $\sim(0.3\text{--}0.4)c$, while in the latter region, the speed is much lower, $\lesssim 0.05c$ (Figure 6). We call the outflow in the first region the “disk jet,” while the outflow in the second region is “wind.” The “disk jet” is different from the Blandford–Znajek jet in several ways, as summarized in Yuan & Narayan (2014). An interesting point is that the disk jet exists even though the black hole is nonrotating. The coexistence of jets and winds is consistent with the detection of winds in radio-loud AGNs (e.g., Tombesi et al. 2010, 2014). In the next step, we will compare the properties of winds predicted by the model with those obtained from observations.
3. For a given test particle, the poloidal speed of the disk jet is found to increase along their trajectory; while for wind, the poloidal speed almost remains constant (Figure 8). This implies that wind can at least escape beyond the outer boundary of the accretion flows. On the other hand, the poloidal speed of the disk jet and wind decreases with increasing radius where they are produced (refer to Equation (8)). This implies that the wind has a mixture of poloidal speed depending on its original launching radius. But the mass-flux-weighted poloidal speed of wind as a function of radius can be described by Equation (7) (Figure 7).
4. The value of Bernoulli parameter Be of the real outflow is not a constant along their trajectories (Figure 9). The physical reason is that the accretion flow is not steady but turbulent. Because of this reason, the value of Be for a real outflow is not necessarily positive.
5. The poloidal speed of outflow does not decrease along the trajectory. This indicates that there must be some acceleration forces. We have analyzed the data and found that in the case of the disk jet, the dominant acceleration force is the gradient of magnetic pressure, while for the wind, the centrifugal force and the gradient of gas and magnetic pressure play comparable roles (Figure 13).
6. We have also calculated the fluxes of energy and momentum of the wind and jet (Figures 11 and 12). Especially, the kinetic energy flux of wind is described by Equation (12). The implied efficiency of wind production is $\epsilon_{\text{wind}} \equiv \dot{E}_{\text{wind}}/\dot{M}_{\text{BH}}c^2 \approx 10^{-3}$, in good agreement with the value required in large-scale AGN feedback simulations.

F.Y. thanks Jim Stone for the valuable discussions. F.Y., Z.G., and D.B. were supported in part by the National Basic Research Program of China (973 Program, grant 2014CB845800), the Strategic Priority Research Program “The Emergence of Cosmological Structures” of CAS (grant XDB09000000), and NSF of China (grants 11103059, 11103061, 11121062, and 11133005). R.N. was supported in part by NSF grant AST1312651 and NASA grant NNX14AB47G. A.S. acknowledges support for this work by NASA through Einstein Postdoctoral Fellowship number PF4-150126 awarded by the *Chandra* X-ray Center, which is operated by the Smithsonian Astrophysical Observatory for NASA under contract NAS8-03060. X.B. is supported by NASA through Hubble Fellowship grant *HST*-HF2-51301.001-A awarded by the Space Telescope Science Institute, which is operated by the Association of

Universities for Research in Astronomy, Inc., for NASA, under contract NAS 5-26555. The authors acknowledge computational support from NSF via XSEDE resources (grant TG-AST080026N), from NASA via the High-End Computing (HEC) Program through the NASA Advanced Supercomputing (NAS) Division at Ames Research Center, and from SHAO Super Computing Platform.

REFERENCES

- Abramowicz, M. A., Igumenshchev, I. V., Quataert, E., & Narayan, R. 2002, *ApJ*, **565**, 1101
- Aitken, D. K., Greaves, J., Chrysostomou, A., et al. 2000, *ApJL*, **534**, L173
- Balbus, S. A., & Hawley, J. F. 1998, *RvMP*, **70**, 1
- Blandford, R. D., & Begelman, M. C. 1999, *MNRAS*, **303**, L1
- Blandford, R. D., & Begelman, M. C. 2004, *MNRAS*, **349**, 66
- Blandford, R. D., & Payne, D. G. 1982, *MNRAS*, **199**, 883
- Blandford, R. D., & Znajek, R. L. 1977, *MNRAS*, **179**, 433
- Begelman, M. C. 2012, *MNRAS*, **420**, 2912
- Bower, G. C., Wright, M. C. H., Falcke, H., & Backer, D. C. 2003, *ApJ*, **588**, 331
- Ciotti, L., Ostriker, J. P., & Proga, D. 2010, *ApJ*, **717**, 708
- Crenshaw, D. M., & Kraemer, S. B. 2012, *ApJ*, **753**, 75
- Crenshaw, D. M., Kraemer, S. B., & George, I. M. 2003, *ARA&A*, **41**, 117
- Debuhr, J., Quataert, E., Ma, C.-P., & Hopkins, P. 2010, *MNRAS*, **406**, L55
- Fabian, A. C. 2012, *ARA&A*, **50**, 455
- Gan, Z., Yuan, F., Ostriker, J. P., Ciotti, L., & Novak, G. S. 2014, *ApJ*, **789**, 150
- Gaspari, M., Brighenti, F., & Temi, P. 2012, *MNRAS*, **424**, 190
- Gu, W. M. 2014, *ApJ*, in press (arXiv:1411.3965)
- Hawley, J. F., & Balbus, S. 2002, *ApJ*, **573**, 738
- Hawley, J. F., & Krolik, J. 2006, *ApJ*, **641**, 103
- Hawley, J. F., Gammie, C. F., & Balbus, S. A. 1995, *ApJ*, **440**, 742
- Igumenshchev, I. V. 2002, *ApJL*, **577**, L31
- Igumenshchev, I. V., & Abramowicz, M. A. 1999, *MNRAS*, **303**, 309
- Igumenshchev, I. V., & Abramowicz, M. A. 2000, *ApJS*, **130**, 463
- Igumenshchev, I. V., Narayan, R., & Abramowicz, M. A. 2003, *ApJ*, **592**, 1042
- Kato, Y., Mineshige, S., & Shibata, K. 2004, *ApJ*, **605**, 307
- King, A. 2003, *ApJL*, **596**, L27
- Komissarov, S. S. 2001, *MNRAS*, **326**, L41
- Kormendy, J., & Ho, L. C. 2013, *ARA&A*, **51**, 511
- Li, J., Ostriker, J., & Sunyaev, R. 2013, *ApJ*, **767**, 105
- Lynden-Bell, D. 2003, *MNRAS*, **341**, 1360
- Marrone, D. P., Moran, J. M., Zhao, J. H., & Rao, R. 2007, *ApJL*, **654**, L57
- McKinney, J. C. 2005, *ApJL*, **630**, L5
- Mou, G., Yuan, F., Bu, D., Sun, M., & Su, M. 2014, *ApJ*, **790**, 109
- Narayan, R., Igumenshchev, I. V., & Abramowicz, M. A. 2000, *ApJ*, **539**, 798
- Narayan, R., Igumenshchev, I. V., & Abramowicz, M. A. 2003, *PASJ*, **55**, L69
- Narayan, R., Sadowski, A., Penna, R. F., & Kulkarni, A. K. 2012, *MNRAS*, **426**, 3241
- Narayan, R., & Yi, I. 1994, *ApJL*, **428**, L13
- Narayan, R., & Yi, I. 1995, *ApJ*, **452**, 710
- Novak, G. S., Ostriker, J. P., & Ciotti, L. 2011, *ApJ*, **737**, 26
- Ostriker, J. P., Choi, E., Ciotti, L., Novak, G. S., & Proga, D. 2010, *ApJ*, **722**, 642
- Pen, U.-L., Matzner, C. D., & Wong, S. 2003, *ApJL*, **596**, L207
- Penna, R. F., Kulkarni, A., & Narayan, R. 2013a, *A&A*, **559**, A116
- Penna, R. F., Narayan, R., & Sadowski, A. 2013b, *MNRAS*, **436**, 3741
- Pringle, J. E. 1981, *ARA&A*, **19**, 137
- Quataert, E., & Gruzinov, A. 2000, *ApJ*, **539**, 809
- Sadowski, A., Narayan, R., Penna, R., & Zhu, Y. 2013, *MNRAS*, **436**, 3856
- Shakura, N. I., & Sunyaev, R. A. 1973, *A&A*, **24**, 337
- Shibata, K., & Uchida, Y. 1985, *PASJ*, **37**, 31
- Stone, J. M., & Pringle, J. E. 2001, *MNRAS*, **322**, 461
- Stone, J. M., Pringle, J. E., & Begelman, M. C. 1999, *MNRAS*, **310**, 1002
- Tehekhsokoy, A., McKinney, J. C., & Narayan, R. 2012, *JPhCS*, **372**, 012040
- Tehekhsokoy, A., Narayan, R., & McKinney, J. C. 2010, *ApJ*, **711**, 50
- Tehekhsokoy, A., Narayan, R., & McKinney, J. C. 2011, *MNRAS*, **418**, L79
- Tombesi, F., Sambruna, R. M., Reeves, J. N., et al. 2010, *ApJ*, **719**, 700
- Tombesi, F., Tazaki, F., Mushotzky, R. F., et al. 2014, *MNRAS*, **443**, 2154
- Wang, Q. D., Nowak, M. A., Markoff, S. B., et al. 2013, *Sci*, **341**, 981
- Yuan, F., Bu, D. F., & Wu, M. C. 2012a, *ApJ*, **761**, 130
- Yuan, F., & Narayan, R. 2014, *ARA&A*, **52**, 529
- Yuan, F., Quataert, E., & Narayan, R. 2003, *ApJ*, **598**, 301
- Yuan, F., Wu, M. C., & Bu, D. F. 2012b, *ApJ*, **761**, 129